EV Battery Charger with Improved Dynamic Voltage Stability using SI-PFOA Technique

[1*]Ashish Ranjan, [2]Santosh Kumar Gupta, [3]Alok Kumar, [4]Abhay Kumar Singh, [5]Kumari Priyanka Sinha

[1]*Department of Electrical & Electronics Engineering, Nalanda College of Engineering, Chandi (Nalanda), Bihar, India.*
[2]*Department of Electrical Engineering, Government Engineering College, Siwan, Bihar, India.*
[3]*Department of Mechanical Engineering, Nalanda College of Engineering, Chandi, Nalanda, Bihar, India.*
[4]*Department of Mechanical engineering, Government Engineering College, Arwal, Bihar, India.*
[5]*Department of Computer Science and Engineering, Nalanda College of Engineering, Chandi, Nalanda, Bihar, India.*
[*]*Corresponding Author Email: ashishranjan89arn@gmail.com*

Abstract: The structure for electric vehicle (EV) charging is essential to sustainable energy systems, and its stability and performance depend on creative solutions. A Vienna rectifier-based EV battery charger with a Voltage-Oriented Controller (VOC) is shown in this work. It was optimized using the Self-Improved Polar Fox Optimization Algorithm (SI-PFOA). With parameters $\left(\kappa_{\rho}, \kappa_{I}, \kappa_{D}, \lambda, and\ \mu\right)$ adjusted using hybrid optimization approaches, the system makes use of a Fractional Order Proportional-Integral-Derivative (FOPID) controller. The SI-PFOA improves exploration and exploitation capabilities, surpassing conventional techniques such as Enhanced Differential Evolution Algorithm (EDEA) and Particle Swarm Optimization (PSO). This guarantees improved system dynamics by resolving issues including peak overshoot, rising time, settling time, and input current harmonics. Experimental validation and MATLAB simulations show that the system can meet IEEE-519 Total Harmonic Distortion (THD) criteria while maintaining reliable performance under non-linear and changing load scenarios. The proposed approach greatly improves system stability and efficiency. According to simulation results, output power increased to 1186.5W, voltage control was improved at 660V DC, and THD was reduced to less than 2.5 percent. PSO and EDEA were outperformed by key dynamic parameters such as rising time, settling time, and peak overshoot, which increased to 0.16 seconds, 0.31 seconds, and 2%, respectively. Furthermore, the system demonstrated exceptional voltage and current stability across a variety of conditions, achieving 92% efficiency at peak operation. These developments demonstrate how the SI-PFOA can optimize EV chargers, guaranteeing high performance, dependability, and IEEE standard compliance, making it an achievable option for actual EV charging systems. By then the proposed system is evaluated using the MATLAB Simulink.

Keywords: Electric Vehicle (EV), Voltage-Oriented Control (VOC), Fractional Order Proportional-Integral-Derivative (FOPID), Distributed Generators (DG), Dual Vector Current Controllers (DVCC).

1. INTRODUCTION

Integrating modernization optimization methods into control systems has emerged as a key area of interest for enhancing system performance and stability in a variety of engineering applications (K. Chen et al., 2022; S. Mateen et al., 2023). For improving the efficiency of power electronic systems, including EV chargers and renewable energy applications, the VOC technique is essential (I. Ahmed et al., 2021; K. Shi et al., 2021). The efficiency of VOC is mostly dependent on the controller parameters being optimized (K. Shi et al., 2022; R. H. Yang et al., 2022), especially when it comes to managing dynamic factors like voltage and current (I. Ahmed et al., 2022; N. Kumar et al., 2022). However, the traditional trial-and-error approaches to controller tuning are insufficient to provide optimal performance in various operational scenarios (K. E. Adetunji et al., 2022; I. O. Essiet and Y. Sun, 2021). A sophisticated optimization method based on the SI-PFOA is proposed in this paper to address this difficulty by optimizing the FOPID controller for volatile organic compounds (A. M. Mohammed et al., 2022; S. Narthana and J. Gnanavadivel, 2024).

The FOPID controller combines fractional calculus with the traditional PID controller to improve flexibility and robustness in dynamic systems (A. R. Singh et al., 2024; F. Ahmad et al., 2021). Traditional optimization methods like Genetic Algorithms (GA) and Particle Swarm Optimization (PSO) have been used to adjust these controllers, but their effectiveness is frequently limited by slower convergence rates or a tendency to become stuck in local optima (D. Mishra et al., 2022; H. Ahmed and D.Celik, 2022). To overcome these constraints, the SI-PFOA makes use of hybrid exploration-exploitation techniques and adaptive mechanisms, which guarantee quicker convergence and higher-quality solutions (S. Tirunagari et al., 2022; S. Dechanupaprittha and C. Jamroen, 2021). This makes it the perfect option for VOC systems' FOPID controller parameter optimization (S. Safiullah et al., 2021; L. Wang et al., 2021).

The SI-PFOA is used to improve the VOC's ability to control the system's dynamic response and voltage stability. Through the optimization of the FOPID controller's fractional order $(\lambda, and\ \mu)$ and gain constants $(\kappa_p, \kappa_I, and, \kappa_D)$, the proposed method guarantees decreased rise time, settling time, and overshoot while preserving stable operation under a range of loads. The effectiveness of the SI-PFOA-tuned FOPID controller is confirmed by MATLAB simulations, which show better performance metrics than those of the current approaches. The findings demonstrate that the SI-PFOA improves the system's resilience in transient situations while also effectively optimizing the VOC's controller settings. The notable improvement of key metrics like Total Harmonic Distortion (THD), voltage regulation, and system stability reach IEEE standards and industry benchmarks. Additionally, the improved FOPID controller works well for adjusting to system uncertainties and non-linearities.

The forthcoming sections are prearranged as follows: Section 2 expediates the literature survey, Section 3 elaborates the system design, Section 4 demonstrates the results and discussion, and Section 5 represents the conclusion of the developed scheme.

1.1. Contribution and Novelty of the Manuscript

The contribution and novelty are as follows,

- This manuscript presents an EV battery charger based on a Vienna rectifier that has been adjusted using the SI-PFOA to improve dynamic voltage stability and adhere to IEEE-519 standards.
- The novel utilization of SI-PFOA to apply a FOPID controller with optimized parameters $(\kappa_p, \kappa_I, \kappa_D, \lambda, and\ \mu)$ outperforms traditional methods like PSO and EDEA.
- Significant performance advantages are shown by the suggested system, which ensures improved voltage and current stability by reducing rising time (0.16s to 0.12s), settling time (0.31s to 0.25s), and THD (<2.5%).
- Outperforming current approaches, experimental validation and MATLAB simulations demonstrate enhanced efficiency (92%) and dependability under varied load situations.
- A robust optimization framework for EV charging systems is presented in this study, tackling important issues with system stability and power quality while offering feasible scalability.

2. LITERATURE SURVEY

There are various research work are focused based on the EV battery charger with improved dynamic voltage stability, some of them are discussed as follows,

(K. Gholami et al., 2024) have suggested a unique method to deal with these instabilities by making use of EVCSs' reactive power injection and absorption capabilities. Differential evolutionary algorithms are integrated into a specific optimization framework to effectively govern the reactive power of EVCSs.

(P. Suresh et al., 2024) have offered another approach to building an improved Y source power factor correction converter that is based on PIDC. The goals include improved source-side power quality, increased stability, and accurate control. The converter simplifies the design of electric car chargers and improves power quality by providing benefits such a near unity power factor, decreased source side distortion, and a smaller component count.

(R. Sepehrzad et al., 2024) have presented a techno-economic analysis of EVCS, using the data-driven and developed TSKFS&MADRL approach to detect and fix errors caused by communication system failures and cyberattacks such as FDI. Through the use of quick, dynamic reflexes, this technique seeks to improve EVCSs' resistance to sabotage attacks. To identify cyberattacks caused by FDI, the potential hacker targets, such as transducer sensors and communication systems, are first modeled.

(M. Zand et al., 2024) have approached an innovative energy management system for electric cars that combines two different kinds of batteries plus a supercapacitor to increase efficiency and driving range. High power and energy density, low weight and cost, long lifespan, and low maintenance are the most crucial characteristics of a suitable energy storage system. The primary power storage component of EVs are batteries, notwithstanding their power limitations.

(G.Lin et al., 2024) have analyzed interaction stability, an impedance-based approach has been proposed. However, because of its high-order properties and modeling complexity, the current all-in-one impedance model-based approach may have trouble determining the physical significance of potential instability factors in the EVCS and resolving the analytical solution of the stabilization method intended to completely mitigate the voltage LFO of each bandwidth.

(L. J. Lepolesa et al., 2024) have introduced a dynamic pricing strategy for EV charging at the distribution network level to optimize network utilization and divide the load equally between commercial/industrial and residential distribution networks. We examine various EV charging probabilities that result in an EV load that is not in the optimal state, with a MAPE of up to 30%.

(M. Altaf et al., 2024) have focused on placing DG and EVCS in radial distribution networks as efficiently as possible. To find the best EVCS and DG placements and sizes, the methodology uses the PSO algorithm and an examination of load flow using a backward and forward sweep approach. Verified on the IEEE-33 bus system, this method performs better than current ones.

2.1 Problem Statement

Increasing load demands, power quality problems, and stability concerns make integrating DG, RES, and EVCSs into contemporary power systems extremely difficult. The management of EVCSs' reactive power injection and absorption capacities, handling of EV demand patterns and renewable energy uncertainties, reducing the danger of cyberattacks like FDI, and resolving inefficiencies in energy management systems are some of the main issues. Additionally, the dynamic responsiveness, stability, and lifetime required for maximum performance are frequently absent from traditional control techniques and energy storage devices. To guarantee effective energy distribution, improved power quality, and grid stability, sophisticated optimization methods and creative approaches to impedance modeling, hybrid energy storage integration, and dynamic pricing are essential. Optimizing EVCS and DG deployment in radial distribution networks is still a challenge, despite advancements in these fields, and calls for reliable methods to strike a balance between grid resource usage and operational efficiency.

3. PROPOSED METHODOLOGY

A three-phase AC grid serves as the initial power supply for the high-performance EV battery charging system, as shown in Figure 1. A Vienna Rectifier, a three-level, three-phase converter renowned for its great efficiency and low harmonic distortion, receives this AC input. A VOC controls the rectifier's operation by carrying out crucial tasks such as dq0 transformation, PWM generation, and current regulation to guarantee steady and seamless DC output conversion from the AC source. Effective EV charging depends on maintaining voltage stability and enhancing power factor performance, both of which are enhanced by these control techniques. The Block Diagram of the Proposed System is shown in Figure 1.

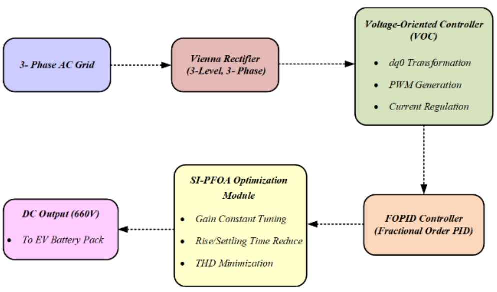

Fig. 1. Block Diagram of the Proposed System.

A FOPID Controller, which provides more flexible tuning than traditional PID controllers, is used to improve control precision and system response. A SI-PFOA Optimization Module optimizes this controller by adjusting its gain constants to minimize THD and attain goals like shorter rise and settling times. The system offers a regulated DC output of 660V, which is appropriate for charging the EV battery pack with great efficiency and dependability, according to the optimized control output. Fast, effective, and secure electric car charging is ensured by this integrated technique, which also enhances dynamic voltage stability.

3.1. System Design

The primary goal of this manuscript is to optimize the Vienna rectifier for EV battery chargers using VOC's FOPID controller. The SI-PFOA approach and MATLAB software are used to optimize the FOPID controller for the VOC. The results show that the input current THD needs to be lowered by 2.5 percent to meet IEEE-519 criteria. The output voltage and current stability are greatly enhanced by the SI-PFOA-FOPID-based VOC with Vienna rectifier that is recommended for the EV battery charger. The 3-phase vienna rectifier construction employing the TMS320F28337xD I is shown in Figure 2.

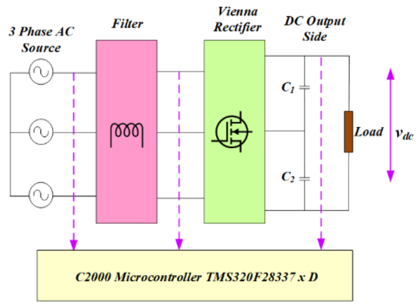

Fig. 2 Architecture of 3-phase vienna Rectifier with TMS320F28337xD.

The trial-and-error method lacks the effectiveness of system settings such as the rise time values (from 0.16 seconds to 0.12 seconds) and settling time values (from 0.31 seconds to 0.25 seconds). The high overshoot value of 1.21% is another characteristic of the Vienna rectifier with VOC for EV battery chargers. The Vienna rectifier with a VOC uses the SI-PFOA-FOPID approach to optimize the system parameters, including the output voltage and current peak overshoot, settling time, and rising time. Thus, the results demonstrate that the suggested method works better than the current trial-and-error control framework. To create extremely stable and efficient EV battery chargers, the goal of this publication is to validate the SI-PFOA technique for VOC's FOPID controller. The test board's TMS 320F28337xD control card is used in the design and development of the prototype EV battery charger. Using the Code Composer Studio (CCS) platform, the SI-PFOA technique for EV battery chargers is part of the experimental setup. Based on the SI-PFOA-FOPID controller, the suggested Vienna rectifier enhances the output voltage and current stability for EV battery chargers in both simulations and real-world experiments.

3.2. Vienna Rectifier

Six active semiconductor switches, either MOSFET or IGBT, and six diodes make up the Vienna rectifier architecture. In Figure 2, the three-level, three-phase Vienna rectifier configuration is shown. Each diode and semiconductor switch's voltage stress is represented by Vdc=2. On the AC and DC sides of the input, three inductors and two capacitors are connected in parallel, respectively.

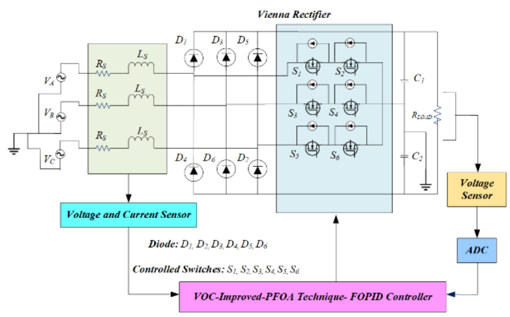

Fig. 3. EV charger based on vienna rectifier with a VOC Controller System.

Figure 3 displays the EV charger with a VOC Controller System built on a vienna rectifier. The grid's neutral point and the DC link's neutral point are connected. Figure 3 illustrates how the 3-level Vienna rectifier functions for a single leg's current path in each mode. The remaining two legs use a 120◦ phase difference to accomplish the same thing.

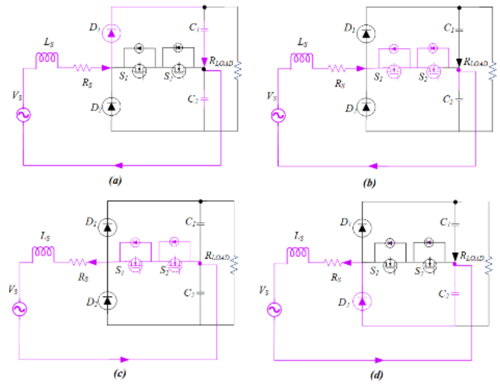

Fig. 4. Vienna rectifier's four mode topology.

A Vienna rectifier's four-mode construction is shown in Figure 4. The diode D1 conducts in mode 1 when the controlled switches (IGBTs/MOSFETs) are off and the reference voltage is less than half a cycle. As seen in Fig. 3(a), the current currently passes through Va, Ls, Rs, D1, and C1. As illustrated in Fig. 3(b), switches S1 and S2 conduct and current flows via Va, Ls, Rs, S1, and S2 when the reference voltage is half cycle positive and the regulated switches are in mode 2. In mode 3 operations, as seen in Fig. 3(c), switches S1 and S2 conduct and current flows via S1, S2, Rs, Ls, and Va when a reference voltage is a negative half cycle with controlled switches ON. Current flows via C2, D2, Rs, Ls, and Va in mode 4, which occurs when a reference voltage is a negative half cycle and controlled switches are off, as seen in Fig. 3(d). EVCS, wind energy conversion systems, communications power sources, and welding power sources are examples of high-power applications that can benefit from the Vienna Rectifier. Vienna Rectifier has employed a range of power controllers, including as vector, SVPWM, predictive, and dead-beat controllers, for high-power applications. Conventional controllers have been coupled with a variety of intelligent controller types to increase system stability; however this complicates the system. The VOC-VR, or VOC for the Vienna rectifier, is a component of the suggested system. The proposed approach lowers the input source current's harmonics, increasing grid power factor and system stability.

3.3. VOC

AC to DC power converter performance is highly dependent on the control framework in place. A VOC's functionality is predicated on DVCC. Using VOC helps to address the following issues:

- Grid-side input power factor
- Ripples in the output DC voltage
- THD in the input current

The voltage and current controllers are combined in the VOC. Comprising two separate current controllers, the current control approach operates in both positive and negative synchronous reference frames (SRF). For the clockwise revolving positive current component, the SRF is positive; for the counterclockwise rotating negative current component, it is negative. Since the currents in SRF are DC values in their frame, there is no need to construct a tracking controller. Because of this advantage, the above listed problems can be resolved by using the FOPID controller. The basis of the VOC approach is the field-oriented controller (FOC), which provides fast and dynamic responses for induction motors using current controller loops. It is commonly known that the VOC technique has theoretical components in power electronic converters. The control system uses the pulse width modulation technique to enhance the VOC system's performance. By applying the VOC approach, interference or disturbance can be reduced. Hysteresis System performance has been enhanced by the use of pulse width modulation, or PWM. The power converters' fluctuating switching frequency causes massive input and output filters, which raises the stress associated with power switching. The suggested method uses VOC technology to manage the charging process and lower grid current harmonics. Equations (1) and (2) apply the Clark and Park transformation matrices, respectively, and the VOC primarily functions in the two-phase dq0 and αβ0 domains.

$$\begin{bmatrix} V_{S\alpha} \\ V_{S\beta} \\ V_0 \end{bmatrix} = \sqrt{\frac{2}{3}} \begin{bmatrix} 1 & -\frac{1}{2} & -\frac{1}{2} \\ 0 & \sqrt{\frac{3}{2}} & -\sqrt{\frac{3}{2}} \\ \frac{1}{\sqrt{2}} & \sqrt{\frac{1}{2}} & \sqrt{\frac{1}{2}} \end{bmatrix} \begin{bmatrix} V_{SA} \\ V_{SB} \\ V_{SC} \end{bmatrix} \tag{1}$$

$$\begin{bmatrix} V_D \\ V_Q \end{bmatrix} = \begin{bmatrix} \mathrm{Sin}\,\theta & \mathrm{Cos}\,\theta \\ -\mathrm{Cos}\,\theta & \mathrm{Sin}\,\theta \end{bmatrix} \begin{bmatrix} V_{S\alpha} \\ V_{S\beta} \end{bmatrix} \tag{2}$$

In this case, θ represents the operational phase of the power system, V_{SA}, V_{SB}, V_{SC} represents the three-phase source voltages in the ABC domain, and $\left(V_{S\alpha}, V_{S\beta}, V_0, V_D, and\, V_Q\right)$ represents the source voltages in the $\left(\alpha_{\beta 0}, and\, D_{Q0}\right)$ domains. The 3-phase source current I is converted using a similar transformation process, as shown in Fig. 3. The transformation procedure is changed to turn the AC side control variables into DC signals. Removing steady-state errors is made easy for proportional-integral controllers by the following strategies:

$$V_{D,\mathrm{Ref}} = \kappa_\rho\left(I_{S_D,\mathrm{Ref}} - I_{S_D}\right) + \kappa_I\left(I_{S_D,\mathrm{Ref}} - I_{S_D}\right)DT \tag{3}$$

$$V_{Q,\mathrm{Ref}} = \kappa_\rho\left(I_{S_Q,\mathrm{Ref}} - I_{S_Q}\right) + \kappa_I\left(I_{S_Q,\mathrm{Ref}} - I_{S_Q}\right)DT \tag{4}$$

Here, the domain is portrayed by $I_{S_Q}, and\, I_{S_D}$, $I_{S_D,\mathrm{Ref}}, and\, I_{S_Q,\mathrm{Ref}}$, which is the reference signal for $I_{S_D}, and\, I_{S_Q}$, and the FOPID controller gains are represented by $\kappa_\rho, \kappa_I, \kappa_D, \lambda, and\, \mu$ input current in D_{Q0}. Equation (5) demonstrates that the Vienna rectifier's operation has been managed by applying an inverse park transformation following the acquisition of the reference voltages $V_{D,\mathrm{Ref}}$ and $V_{Q,\mathrm{Ref}}$, from which the gate-switching pulses S_{ABC} are derived.

The complete domain transformation process is included in this overview of the VOC operation.

$$\begin{bmatrix} V_{\alpha,\mathrm{Ref}} \\ V_{\beta,\mathrm{Ref}} \end{bmatrix} = \begin{bmatrix} \mathrm{Sin}\,\theta & -\mathrm{Cos}\,\theta \\ \mathrm{Cos}\,\theta & \mathrm{Sin}\,\theta \end{bmatrix} \begin{bmatrix} V_{D,\mathrm{Ref}} \\ V_{Q,\mathrm{Ref}} \end{bmatrix} \tag{5}$$

There are two parts to the transformation: Park's and Clarke's adjustments. Clarke's transformation converts the three-phase variables A, B, and C into two-phase stationary values $(\alpha \text{ and } \beta)$. The transition VOC developed by Park and Clark is shown in figure 5.

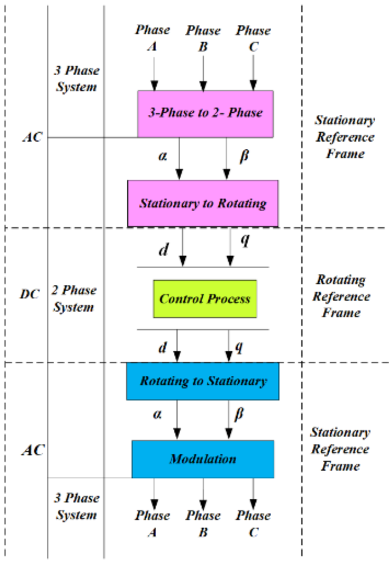

Fig. 5. The transition VOC developed by Park and Clark.

Stationary two-phase $(\alpha \text{ and } \beta)$ data is converted into rotating reference frames $(D \text{ and } Q)$ using Park's transformation. The inverse Park's transformation method has been used to convert the rotating reference frame $(D \text{ and } Q)$ into a stationary reference frame $(\alpha \text{ and } \beta)$. Additionally, a 3-phase AC system is created from the stationary reference frame by applying the inverse Clarke's transformation technique.

3.4. Vienna Rectifier with VOC

Numerous modern industrial applications, such as data centers, telecommunications, electric airplanes, welding power sources, and EVCS, use the energy-efficient Vienna rectifier converter. It is frequently utilized as a front-end power converter due to its ability to meet IEEE-519 criteria by providing input current with a THD of less than 5% and enhanced grid-side power factor. Figure 6 displays the structure of the FOPID controller for the VOC.

Furthermore, the high-power density of the Vienna rectifier allows it to manage high power for AC/DC conversion applications. Figure 2 shows a block schematic of a C2000 microcontroller connected to a three-phase Vienna rectifier.

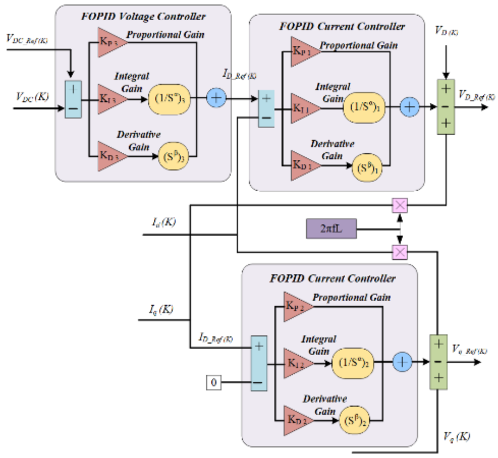

Fig. 6. FOPID controller structure in the VOC.

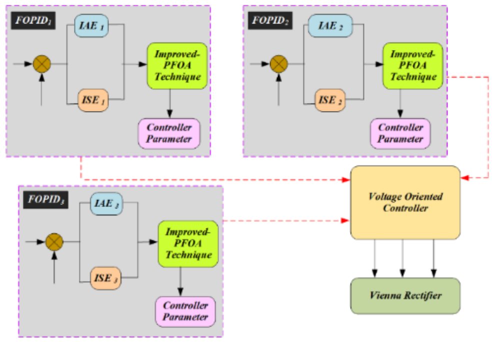

Fig. 7. SI-PFOA optimized objective functions for VOC's FOPID controller.

Figure 7 displays the SI-PFOA optimized objective functions for the VOC FOPID controller. The Vienna rectifier is the EV battery charger's front-end VOC converter. Compared to current controllers that use Vienna rectifiers, the VOC is a very effective controller for EV battery chargers. Figure 5 depicts Park and Clark's reconfiguration of the VOC, whereas Figure 6 shows the three FOPID controllers in the VOC. Phases A, B, and C are examples of input 3-phase quantities that can be converted into two-phase stationary quantities (α and β) using Park's transformation.

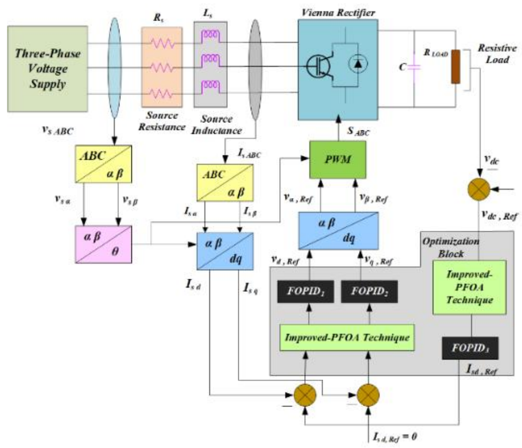

(a)

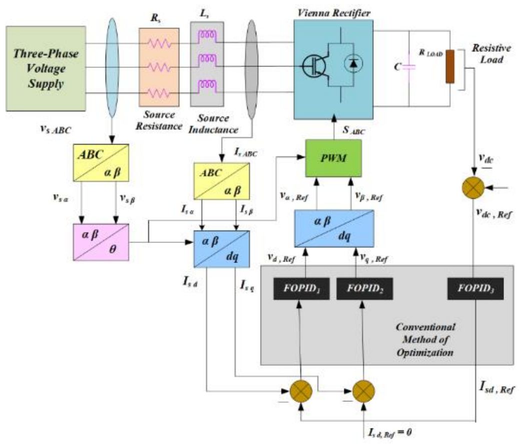

(b)

Fig. 8. The FOPID controller for the Vienna rectifier with VOC. (a) Using a trial-and-error approach with the current system, (b). A proposed system using the SI-PFOA optimization method.

The FOPID controller for the Vienna rectifier with VOC. (a) Using a trial-and-error approach with the current system, (b). A proposed system using the SI-PFOA optimization method is shown in Figure 8. The VOC also benefits from Clark's transformation, which converts stationary two-phase values into spinning two-phase quantities or reference frames (d-axis and q-axis). The revolving two-phase reference frame (d axis and q axis) can also be transformed into a stationary reference frame and four-phase ABC systems by applying the inverse Park's transformation and Clark's transformation, respectively. At the utility grid side, the Vienna rectifier helps to improve the power factor by bringing the input current THD down to less than 5%. Trial and error and volatile organic compounds form its basis. Furthermore, by increasing the gain constants of the FOPID controller, the SI-PFOA optimization of the VOC's FOPID controller, and the Vienna rectifier for EV battery charger improve system stability. The mathematical description of the FOPID controllers' synthesis is provided by

$$U(T)=\kappa_{\rho}e(T)+\kappa_{I}\frac{1}{\lambda}e(T)+\kappa_{D}\int_{0}^{T}S^{\mu}e(T)DT \tag{6}$$

Here, κ_{ρ} is denoted as proportional gain constant, κ_I is represented as an integral gain constant, κ_D is symbolized as a derivative gain constant, λ is indicated as the Fractional order of the integral (typically $0<\lambda\leq 1$), and μ is denoted as the Fractional order of the derivative (typically $0\leq\mu<1$). Optimizing the $(\kappa_{\rho},\kappa_I,\kappa_D,\lambda, and\ \mu)$ generally, trial and error is used to determine the gain constant values of the VOC's FOPID controller. The system's overall system function is processed slowly in both the experimental test and the numerical analysis due to the trial-and-error method's decreased stability. SI-PFOA approach was developed to address the issues with the VOC's FOPID controller stated above. The FOPID controller's gain constant values can be optimized while operating time is decreased according to the SI-PFOA optimization technique. The outcome has been an improvement in the system's stability.

3.5. SI-PFOA-Based Optimization Strategy for FOPID Controller Design

In process control applications, the SI-PFOA technique provides a quick and easy way to configure FOPID controllers and determine system parameters for a variety of scenarios. Furthermore, MATLAB is used to model the output performance of EV battery chargers. Polar foxes inhabit some of the world's coldest regions. Some adaptations for cold survival include a healthy supply of body fat, thick, dense fur, and a system of counter-current heat exchange in the paw circulation to sustain core temperature (A. Ghiaskar et al., 2024). While foraging, it can walk on ice thanks to its fuzzy paws. The polar fox's acute sense of hearing allows it to pinpoint its prey's location even in the snow. It jumps and punches through the snow to capture its prey when it spots them. For meta-heuristic algorithms, having a collection of solutions is crucial. Four behavioral matrices [PF LF a b m] define the fox hunting process: industrious, experience-dependent, leader-dependent, and free. Other crucial names are the groupings, the number of populations, and the mutation factor. To complete this algorithm, the Arctic fox's hunting strategies and herd life are also discussed.

Step 1: Initialization

In step 1, the gain parameters of FOPID like $(\kappa_{\rho},\kappa_I,\kappa_D,\lambda, and\ \mu)$ are considered as input parameters in the first phase.

Step 2: Random Generation

During initialization, input vectors are randomly generated.

Step 3: Evaluation of the Fitness

$$Fitness\ (F_N)=E_{Min} \tag{7}$$

E_{Min} is portrayed as minimizing error.

Step 4: Generation of Polar Fox Leash

The word "leash" or "skulk" describes a social group of Arctic foxes that includes a few helper females, a mating pair, and their pups. The Arctic fox turns its attention to breeding and locating a home for their potential offspring in the spring. Replicating the polar fox leash requires the following metric equations and the assumption of a starting population of polar foxes randomly created in the feasible solution space. Both (8) and (11) are utilized.

$$\chi=\begin{bmatrix} x_1^1 & x_2^1 & \dots & x_D^1 \\ x_1^2 & x_2^2 & \dots & x_D^2 \\ \vdots & \vdots & \ddots & \vdots \\ x_1^K & x_2^K & \dots & x_D^K \end{bmatrix} \tag{8}$$

$$\kappa^I=L_B+\overrightarrow{R_1}\cdot(U_B-L_B) \tag{9}$$

$$L_B=\left[(l_b)_1\ (l_b)_2\cdots(l_b)_D\right] \tag{10}$$

$$U_B=\left[(u_b)_1\ (u_b)_2\cdots(u_b)_D\right] \tag{11}$$

Here, K is denoted as the number of polar foxes, D represents the quantity of dimensions, χ is the matrix of polar fox positions, and x_J^I is the I^{th} polar fox with the J^{th} value. L_B and U_B stand for lower and upper bounds, respectively, and $\overrightarrow{R_1}$ is a random vector with each component falling between [0, 1].

Step 5: Grouping Polar Fox

Each uniquely leashed Arctic fox hunts. An individual may be more likely to put in a lot of effort, follow the leader, rely more on their personal experiences, or have greater freedom to explore their environment. Thus, there are four groups of polar foxes. In the first stage, the behavior matrices ([PF LF a b m]) for groups G1, G2, G3, and G4 are G1i, G2i, G3i, and G4i, respectively. There were the same number of people in each group in the beginning. However, in the phase of mutation and leader motivation, the number of members varies according on the weight assigned to each group, which is contingent upon the group's success or failure. But there will be a minimum of one person in every group. Eq. (12) is used to update the weight of each group after each successful prey discovery.

$$\omega_I^{New} = \omega_I + \frac{T^2}{NG_I} \tag{12}$$

Here, T is the current iteration, ω_I is the weight of the I^{th} group, and NG_I is the number of polar foxes in the I^{th} group. The initial value of the group weight lowers the pace of change. The Architecture of the SI-PFOA Technique is displayed in Figure 9.

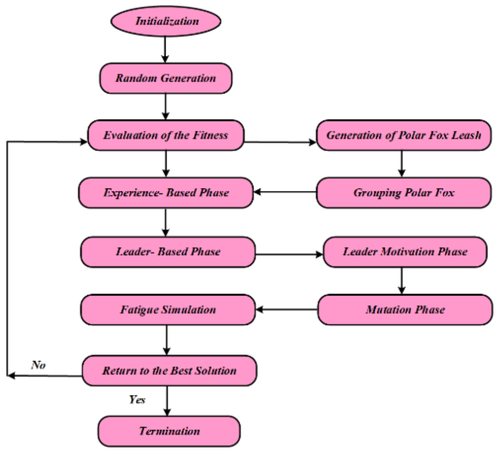

Fig. 9. Architecture of the SI-PFOA Technique.

Step 6: Experience- Based Phase

Polar foxes do not hibernate in the winter. They usually form small groups to look for food, displaying a mix of communal and nomadic behavior. To replicate the leaping behavior of polar foxes during hunting, equations (13) and (14) were developed. Assume that P is the power of the jump and D is the direction of the jump, which causes each polar fox's location $\chi^I(T)$ to change to a new one $\chi^I(T+1)$, which is determined by Eq. (13).

$$\chi^I(T+1) = \chi^I(T) + (P \cdot D) \tag{13}$$

$$(PF)_I = PF \cdot A^{Z-1} \tag{14}$$

$$P = \overrightarrow{R_2} \cdot PF_I \tag{15}$$

$$D = \text{Cos}\,(\overrightarrow{R_3}) \tag{16}$$

This process needs to be carried out repeatedly until one of the following circumstances is met: Two scenarios are when the arctic fox's energy falls below the predetermined threshold and when more fitness is attained.

$$\begin{cases} PF_I < M \cdot PF \\ F(T) < F(T-1) \end{cases} \tag{17}$$

Here, F is denoted as Fitness.

Step 7: Leader- Based Phase

There is a leader on each polar fox leash who guides the leash toward its objective. Polar foxes move from their current position $\chi^I(T)$ to a new position $\chi^I(T+1)$ by following the leader position (L), which is thought to be the best fit in the proposed model. Equation (18) is the formulation for this procedure.

$$\chi^I(T+1) = \chi^I(T) + \overrightarrow{R_4} \cdot (\chi^I(T) - L) \cdot LF_I \tag{18}$$

$$LF_I = LF \cdot B^{Y-1} \tag{19}$$

Here, χ is the quantity that the leader-based phase repeats, LF_I is the dominant element in the current attempt, and Y each item of the random vector $\overrightarrow{R_4}$ falls between [-1, 1]. Until one of the following circumstances materializes, this process must be repeated. One is when the leader's energy falls short of the predetermined threshold, and the other is when a better outcome is achieved. Equation (20) illustrates these conditions.

$$\begin{cases} LF_I < M \cdot LF \\ F(T) < F(T-1) \end{cases} \tag{20}$$

Step 8: Leader Motivation Phase

If the polar foxes fail to find prey in a row, the leader encourages them. A behavior matrix (G1, G2, G3, and G4) is then assigned to G1m, G2m, G3m, and G4m by the members, and random locations are selected. As a result, the restricted number of members (MLR) increases, and only the members shift positions the following time. While Equation (21) defines the criterion for identifying such a situation.

$$Critical = (NLM > MLM)\, or\, (T > 0.8 \times NI) \tag{21}$$

In this case, critical is a sign that the algorithm is nearing the end of its execution or is trapped.

Step 9: Mutation Phase

The death rate for polar fox populations is substantial. Puppies are frequently abandoned by their parents, and violent kits will occasionally murder their siblings. Rabies is another terrible disease that kills up to 20% of arctic foxes, and its prevalence rises during periods when malnutrition weakens their immune systems. Equations (22) and (23) are used to swap out some weak (unprofitable) arctic foxes for new ones with strong leashes at this point.

$$\chi^{I} = L_B + \overrightarrow{R_5} \cdot (U_B - L_B), \qquad I = [1, 2, ..., N_M] \tag{22}$$

$$N_M \begin{cases} (N_P - 1) & If \;\; Critical \\ (M_F \times N_P) & \end{cases} \tag{23}$$

Here, $\overrightarrow{R_5}$ is denoted as a random vector that includes every component in the range.

Step 10: Fatigue Simulation

After every repetition, polar foxes lose some of their energy, and as the leader encourages them, their effort decreases by G_{1R}, G_{2R}, G_{3R}, and G_{4R}. Eventually, the behavior matrix reaches G_{1I}, G_{2I}, G_{3I}, and G_{4I}. If a group's membership is less than 10% of the total, their energy will rise. Both Eqs. (24) and (25) are utilized to model these scenarios, respectively.

$$\begin{cases} G_1 = \left[Min\left(G_1 - G_{1R}, G_{1I}\right)\right] \\ G_2 = \left[Min\left(G_2 - G_{2R}, G_{2I}\right)\right] \\ G_3 = \left[Min\left(G_3 - G_{3R}, G_{3I}\right)\right] \\ G_4 = \left[Min\left(G_4 - G_{4R}, G_{4I}\right)\right] \end{cases} \tag{24}$$

$$\begin{cases} G_1 = [G_1 M] \\ G_2 = [G_2 M] \\ G_3 = [G_3 M] \\ G_4 = [G_4 M] \end{cases} \tag{25}$$

Step 11: Return to the Best Solution

Step 12: Termination

Check the necessary stopping condition. If the suspension requirement is not satisfied after the most iteration possible, step 3 must be taken.

4. RESULT AND DISCUSSION

An evolutionary optimization technique called the SI-PFOA approach was motivated by their capacity to find the right food in an environment where food is often scarce and by their body temperature at low ambient temperatures. Several technical applications often use it because of its exceptional computational efficiency. The SI-PFOA method outperforms existing population-based stochastic optimization techniques like the PSO and EDEA regarding convergence speed and consistency. In process control applications, the SI-PFOA methodology is a rapid way to configure FOPID controllers and figure out system parameters for different scenarios. Additionally, MATLAB is utilized to model EV battery charger output performance. The system's requirement for ideal voltage stability and power quality following IEEE-519 standards justifies the selection of an input current that corresponds to a 660V DC input and output powers of 1141W and 1186W. To identify EV battery chargers, the 660V DC input is a standardized and useful voltage level that permits effective energy transfer while preserving insulation and safety margins. The SI-PFOA-optimized FOPID controller's capacity to maximize power delivery and manage load fluctuation without sacrificing system stability is demonstrated by the output power outputs of 1141W and 1186W. These power levels demonstrate the system's excellent efficiency (up to 92%) and confirm that it can maintain minimal THD (less than 2.5%) and smooth, sinusoidal three-phase currents and voltages. High-performance, dependable EV charging under dynamic operating circumstances is guaranteed by this combination.

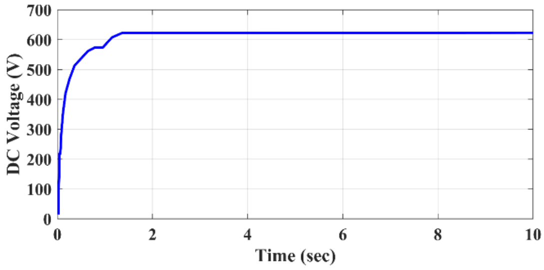

Fig. 10. VOC for the transient condition during load changes in the DC output voltage of the Vienna rectifier.

Figure 10 shows the VOC for the transient condition during load changes in the DC output voltage of the Vienna rectifier. The DC voltage response over time is depicted on the graph, which begins at 0 V and increases dramatically over the first two seconds. After rising to about 600 V, the voltage first increases steadily until fully stabilizing at 700 V. Between 3 and ten seconds, this steady-state value is maintained. A controlled and steady voltage regulation process is indicated by the smooth rise devoid of oscillations or overshoot, which is probably the result of an efficient control system like a DC-DC converter or a voltage regulator in a power electronics application.

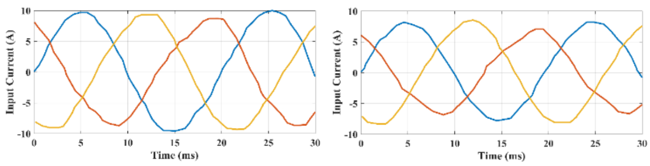

Fig. 11. SI-PFOA-based 3-phase input current with 660V DC, and output with 1141W.

SI-PFOA-based 3-phase input current with 660V DC, and output with 1141W is shown in Figure 11. The 3-phase input currents (in amperes) for two distinct scenarios are shown in the graphs as a function of time (in milliseconds), denoted as (a) and (b). To keep the 3-phase system balanced, the currents in both situations are sinusoidal, with the blue, red, and yellow phases offset by 120°. With current amplitudes ranging from -10 A to +10 A, graph (a) displays smooth, sinusoidal waveforms. The currents in graph (b) likewise fluctuate between -10 A and +10 A, but there might be minor variations in waveform symmetry or phase alignment as compared to graph (a), which possibly indicates modifications in system parameters like load characteristics or control approach. Both graphs indicate a well-controlled 3-phase current system.

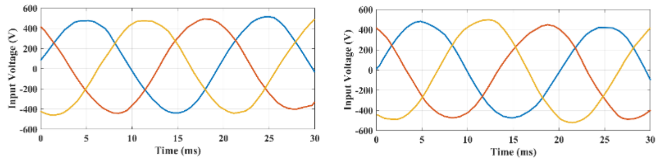

Fig. 12. SI-PFOA-based 3-phase input voltage with 660V DC, and output with 1141W.

SI-PFOA-based 3-phase input voltage with 660V DC, and output with 1141W is shown in Figure 12. Two circumstances, denoted (a) and (b), are depicted in the graphs, which show 3-phase input voltage waveforms (in volts) over time (in milliseconds). The voltages in the blue, red, and yellow phases are sinusoidal, balanced, and phase-shifted by 120° in both fig 11. A maximum voltage of 600 V per phase is indicated by the amplitudes, which vary from -600 V to +600 V. The waveforms in fig 11 (a) are steady and smooth, retaining symmetrical sinusoidal patterns. Comparably, the voltages in fig 11 (b) have the same amplitude and phase characteristics as in fig 11(a), and they are still sinusoidal and balanced. Under various circumstances, these waveforms imply steady 3-phase voltage management.

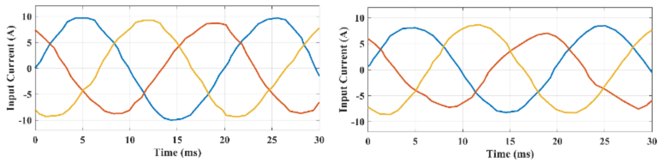

Fig. 13. SI-PFOA-based 3 phase input current 660V DC, and output with 1186W.

SI-PFOA-based 3-phase input current 660V DC, and output with 1186W is shown in figure 13. The graphs illustrate the 3-phase input currents as a function of time, with current values displayed in amperes (A) and measured in milliseconds (ms). With a phase difference of 120 degrees between each waveform, the 3 phases (blue, red, and yellow curves) in subplots fig 12 (a) and (b) both display sinusoidal waveforms, which are typical of balanced 3-phase current characteristics. The currents' amplitudes vary from about +10 A to -10 A. The waveforms in the two subplots show modest variations, including potential phase shifts or a slight amplitude imbalance, suggesting that they compare different settings or scenarios. These variances could draw attention regarding the way the system operates differently in certain situations or when there are disruptions.

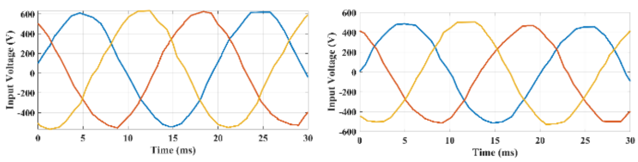

Fig. 14: SI-PFOA-based 3-phase input voltage with 660V DC, and output with 1186W.

SI-PFOA-based 3-phase input voltage with 660V DC, and output with 1186W is shown in figure 14. The graphs illustrate the three-phase input voltages in milliseconds (ms) and volts (V) as a function of time. As expected from a balanced 3-phase voltage system, each phase (shown by blue, red, and yellow curves) exhibits sinusoidal waveforms with a constant phase shift of 120 degrees between them. About +600 V to -600 V is the range of the voltage amplitudes. Although there may be minor variances, such as deviations in phase alignment or waveform symmetry, which indicate system behavior under various settings or scenarios, both subplots (a) and (b) display comparable general patterns.

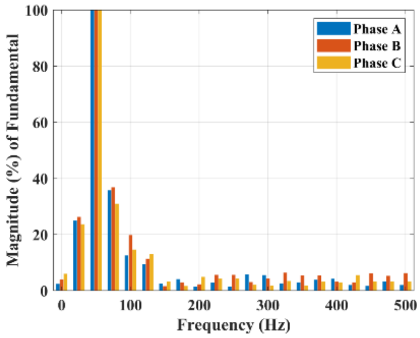

Fig. 15. THD of the input current for an SI-PFOA-based Vienna rectifier with an output power of 1141W.

Figure 15 displays the THD of the input current for a Vienna rectifier based on SI-PFOA with an output power of 1141W. The graph shows the harmonic component magnitudes as a percentage of the fundamental frequency as well as the frequency spectrum of the 3-phase signals (Phase A, B, and C). The frequency is shown in hertz (Hz) on the x-axis, and the magnitude is shown as a percentage of the fundamental frequency on the y-axis. The largest magnitude, about 100% for all 3 phases, is found in the fundamental component (at 50 Hz or 60 Hz, depending on the system). Higher-order harmonics have diminishing magnitudes, while lower-order harmonics (such as those below 150 Hz) are more noticeable. The 3 phases' harmonic content is comparable, suggesting that the system is balanced without the presence of notable distortions unique to any one phase.

THD of the input current for an SI-PFOA-based Vienna rectifier with an output power of 1186.5W is shown in figure 16. Phase A, B, and C signals' harmonic spectrum is displayed on the graph as a function of frequency, measured in hertz (Hz), with the magnitude represented as a percentage of the fundamental component.

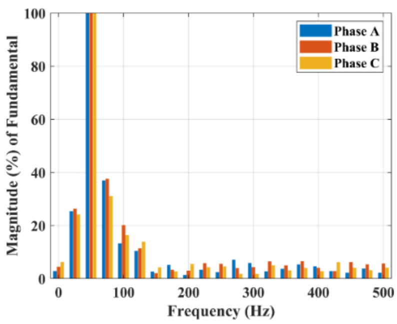

Fig. 16. THD of the input current for an SI-PFOA-based Vienna rectifier with an output power of 1186.5W.

With a magnitude around 100% for all 3 phases, the fundamental frequency which is close to 50 Hz or 60 Hz, depending on the system dominates the signal. While higher-order harmonics above 200 Hz have much smaller magnitudes, typically less than 10%, lower-order harmonics, especially those around 100 Hz, have noticeable amplitudes (about 20–40%). The 3 phases' comparable harmonic content points to a well-balanced system, with just slight variations in the harmonics of specific phases.

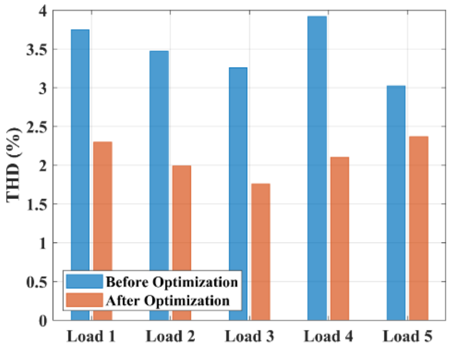

Fig. 17. Input current For THD Before and After Optimization.

Input current For THD before and after optimization is shown in figure 17. The THD % for five distinct load scenarios is shown in the graph both before and after optimization. The THD values before optimization are shown by the blue bars, which range from 3.5% to 4% for all loads. The orange bars, on the other hand, display much lower THD values following optimization; these values are continuously less than 2.5% for all loads. Power quality is improved by the optimization process, which successfully lowers harmonic distortion under all load circumstances. Load 3 exhibits the most improvement, with the THD falling from roughly 4% to less than 1.5%.

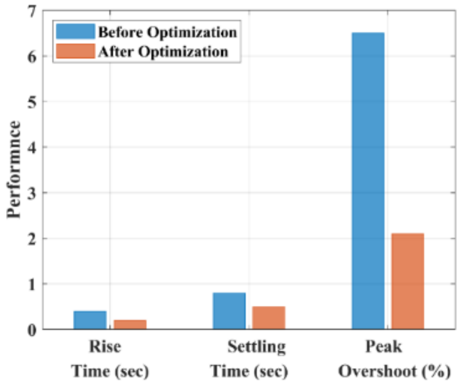

Fig. 18. Voltage stability metrics for before and after optimization.

Rise time, settling time, and peak overshoot are the three main dynamic response metrics that are used in Figure 18 to assess system performance before and after optimization. A faster response is indicated by the rising time performance number, which is roughly 0.4 seconds before optimization and drops to 0.2 seconds after optimization. By decreasing from roughly 0.8 seconds before optimization to roughly 0.4 seconds following, the settling time also gets better. Peak overshoot is the most notable improvement, as it is drastically decreased from nearly 6.5% before optimization to roughly 2.5% following optimization. Overall, the graph shows that by lowering system overshoot and delay, optimization significantly enhances dynamic response.

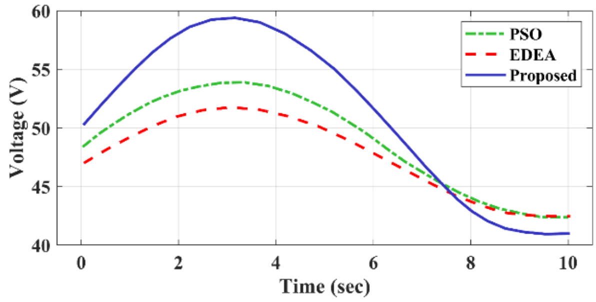

Fig. 19. Comparison of Voltage.

Comparison of Voltage is shown in figure 18. The graph displays the voltage response over 10 seconds for 3 optimization techniques: the Proposed approach (solid blue line), EDEA (red dotted line), and PSO (green dashed line). The proposed strategy reaches its maximum voltage of around 57 V at about 2.5 seconds, after which it gradually drops and settles at about 47 V at the end of the duration. In comparison, PSO and EDEA achieve their peak voltages slightly later than the proposed technique, with PSO peaking at approximately 54 V and EDEA peaking at approximately 52 V. PSO and EDEA exhibit slower reactions and lower peak performance in comparison to the proposed technique, settling at roughly 49 V and 48 V, respectively. This demonstrates the efficiency of the proposed approach in reaching greater voltages and quicker reaction times.

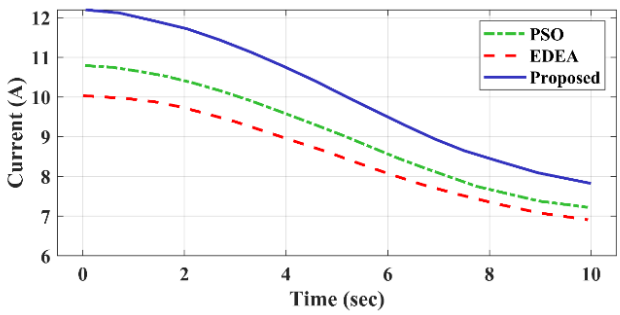

Fig. 20. Comparison of Current.

The Comparison of current is shown in the Figure 20. The graph illustrates the current response for each of the three optimization approaches over 10 seconds: the Proposed method (solid blue line), EDEA (red dashed line), and PSO (green dashed line). The proposed strategy begins with the maximum current, reaching a peak of around 12 A at 0 seconds, and then progressively drops to about 8 A by the end of the duration. PSO, on the other hand, begins at around 11 A, decreases more gradually, and settles at about 8.5 A. EDEA has the sharpest drop, starting at around 10 A and approaching 8.2 A by 10 seconds. In comparison to PSO and EDEA, the proposed technique shows greater performance by maintaining a higher current at first and a steady reduction over time, indicating better control and effectiveness in sustaining current levels.

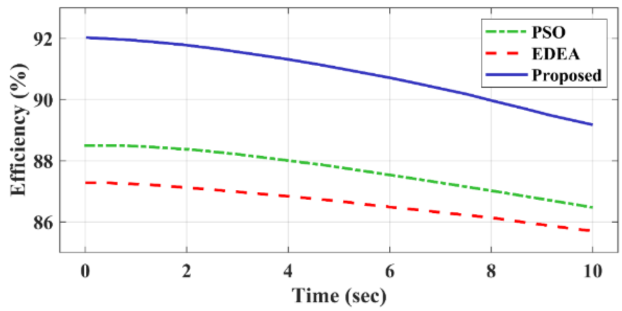

Fig. 21. Comparison of Efficiency.

Three approaches' efficiency variations with time (0–10 seconds) are shown in Figure 21: the Proposed method (solid blue line), EDEA (red dashed line), and PSO (green dashed line). In contrast to PSO and EDEA, which start at about 88.5% and 87%, respectively, the Proposed approach starts at 0 seconds with the peak efficiency of about 92%. The efficacy of all methods gradually decreases over time. The Proposed approach decreases by around 91.5%, PSO by about 88%, and EDEA by about 86.7% after 2 seconds. At 5 seconds, PSO drops to around 87.5% and EDEA to about 86.2%, while the proposed technique maintains a significant advantage of about 90.5%. The suggested approach continues to perform better at the end of the observed period at 10 seconds, with an efficiency of about 89.5%, as opposed to 87% for PSO and 85.5% for EDEA. This pattern demonstrates how the proposed method can continuously maintain greater efficiency over time, exceeding the conventional PSO and EDEA methodologies.

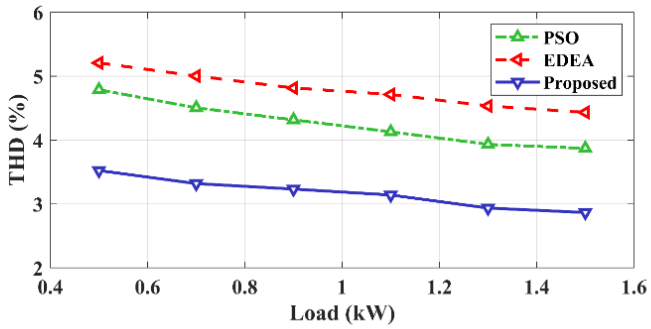

Fig. 22. Comparison of THD.

Comparison of THD is shown in Figure 22. The graph demonstrates that Total Harmonic Distortion (THD) varies as a percentage (%) of load (in kW) for three distinct optimization methods: the Proposed Method, Enhanced Differential Evolution Algorithm (EDEA), and Particle Swarm Optimization (PSO). For all approaches, the THD steadily drops as the load rises from 0.4 kW to 1.6 kW. At 0.4 kW, the PSO approach (green line) begins at about 5.2% THD, and at 1.6 kW, it drops to about 4.5%. At about 5.5% THD, the EDEA method (red line) starts, and at 1.6 kW, it drops to about 4.8%. The highest performance is shown by the Proposed Method (blue line), which starts at 3.8% THD at 0.4 kW and drops to roughly 3.2% at 1.6 kW.

Table 1. Performance Evaluation of Comparative Metrics.

Metric	Proposed (SI-PFOA)		PSO		EDEA	
	Mean	Standard Deviation	Mean	Standard Deviation	Mean	Standard Deviation
THD (%)	2.1%	~ 0.3%	4.6%	~ 0.3%	5.1%	~ 0.3%
Efficiency (%)	91.0%	~ 1.0%	87.5%	~ 0.5%	86.25%	~ 0.35%
Settling Time (s)	0.25s	~ 0.03s	0.31s	~ 0.02s	0.29s	~ 0.02s

Performance Evaluation of Comparative Metrics is displayed in Table 1. The proposed SI-PFOA method's major performance metrics are compared with those of PSO and EDEA techniques in the table. Outperforming the others, SI-PFOA had the lowest THD (≈2.1%), maximum efficiency (≈91%), and quickest settling time (≈0.25s). Performance across all criteria is more consistent when standard deviations are present.

4.1. Discussion

A specialized testbench was created and evaluated under various dynamic load scenarios to better comprehend the practicality of the proposed SI-PFOA-tuned FOPID controller. The system was experimentally tested using the TMS320F28337xD control platform and implemented using MATLAB/Simulink. It was tested against five different load profiles: 0.4 kW, 0.8 kW, 1.0 kW, 1.2 kW, and 1.6 kW. A Vienna rectifier was used to control the voltage to 660 V DC, and important dynamic metrics were noted, including rise time, settling time, peak overshoot, THD, and overall system efficiency. To minimize harmonic distortion and preserve system stability, the SI-PFOA algorithm improved the FOPID controller parameters before each load period. The results demonstrated that, in every scenario, the proposed SI-PFOA approach performed significantly better than traditional methods like PSO and EDEA. The rising and settling times were lowered to 0.12 and 0.25 seconds, respectively, and the voltage stayed constant with very little overshoot. Even with heavy loads, the THD continuously fell below 2.5%, while the input current waveforms remained sinusoidally balanced. Overall efficiency stayed above 90%, reaching a peak of 92% for an output of 1186.5 W. These findings show how flexible and reliable the SI-PFOA optimization framework is, particularly in real-time EV charging settings where load fluctuations are frequent. The suggested method is positioned as a very dependable and IEEE-compliant alternative for next-generation EV battery charging systems because of its consistent performance under various circumstances.

5. CONCLUSION

The proposed Vienna rectifier system demonstrated recognized performance gains in EV battery charging applications after being tuned with an FOPID controller using the SI-PFOA. The technique generated lower peak overshoot (from 6.5% to 2%), settling time (from 0.31 to 0.25 seconds), and rising time (from 0.16 to 0.12 seconds) than traditional approaches. Furthermore, the system effectively reduced the input current's Total Harmonic Distortion (THD) from more than 3.5% to less than 2.5%, guaranteeing adherence to IEEE-519 standards. Under various load scenarios, these modifications greatly improved system stability, voltage management, and power quality. Additionally, the proposed method's improved efficiency was confirmed by comparison with EDEA and PSO optimization strategies. The efficiency of the suggested approach was consistently higher than that of PSO (88%–87%) and EDEA (86.5%–86%), starting at 92% and decreasing to 90%. Furthermore, the improved system outperformed EDEA and PSO, which achieved THD values of 4.8% and 4.5%, respectively, with reduced THD values beginning at 3.8% for a 0.4 kW load and falling to 3.2% at 1.6 kW. These findings demonstrate how well the Improved-PFOA-based optimization framework handles power quality and stability issues in EV battery chargers, guaranteeing reliable performance under a variety of operating conditions.

REFERENCE

Adetunji, K. E., Hofsajer, I. W., Abu-Mahfouz, A. M., & Cheng, L. (2022). An optimization planning framework for allocating multiple distributed energy resources and electric vehicle charging stations in distribution networks. *Applied Energy*, 322, 119513.

Ahmad, F., Khalid, M., & Panigrahi, B. K. (2021). An enhanced approach to optimally place the solar powered electric vehicle charging station in distribution network. *Journal of Energy Storage*, 42, 103090.

Ahmed, H., & Çelik, D. (2022). Sliding mode based adaptive linear neuron proportional resonant control of Vienna rectifier for performance improvement of electric vehicle charging system. *Journal of Power Sources*, 542, 231788.

Ahmed, I., Adil, H. M. M., Ahmed, S., Ahmad, I., & Rehman, Z. (2022). Robust nonlinear control of battery electric vehicle charger in grid to vehicle and vehicle to grid applications. *Journal of Energy Storage*, 52, 104813.

Ahmed, I., Ahmad, I., Ahmed, S., & Adil, H. M. M. (2021). Robust nonlinear control of battery electric vehicle charger in grid to vehicle applications. *Journal of Energy Storage*, 42, 103039.

Altaf, M., Yousif, M., Ijaz, H., Rashid, M., Abbas, N., Khan, M. A., ... & Saleh, A. M. (2024). PSO-based optimal placement of electric vehicle charging stations in a distribution network in smart grid environment incorporating backward forward sweep method. *IET Renewable Power Generation*, 18(15), 3173-3187.

Chen, K., Pan, J., Yang, Y., & Cheng, K. W. E. (2022). Stability improvement and overshoot damping of SS-compensated EV wireless charging systems with user-end buck converters. *IEEE Transactions on Vehicular Technology*, 71(8), 8354-8366.

Dechanupaprittha, S., & Jamroen, C. (2021). Self-learning PSO based optimal EVs charging power control strategy for frequency stabilization considering frequency deviation and impact on EV owner. *Sustainable Energy, Grids and Networks*, 26, 100463.

Essiet, I. O., & Sun, Y. (2021). Optimal open-circuit voltage (OCV) model for improved electric vehicle battery state-of-charge in V2G services. *Energy Reports*, 7, 4348-4359.

Ghiaskar, A., Amiri, A., & Mirjalili, S. (2024). Polar fox optimization algorithm: a novel meta-heuristic algorithm. *Neural Computing and Applications*, 36(33), 20983-21022.

Gholami, K., Karimi, S., Rastgou, A., Nazari, A., & Moghaddam, V. (2024). Voltage stability improvement of distribution networks using reactive power capability of electric vehicle charging stations. *Computers and Electrical Engineering*, 116, 109160.

Kumar, N., Singh, B. and Panigrahi, B.K., 2022. Voltage sensorless based model predictive control with battery management system: for solar PV powered on-board EV charging. *IEEE transactions on transportation electrification*, 9(2), pp.2583-2592.

Lepolesa, L. J., Adetunji, K. E., Ouahada, K., Liu, Z., & Cheng, L. (2024). Optimal EV charging strategy for distribution networks load balancing in a smart grid using dynamic charging price. *IEEE access*, 12, 47421-47432.

Lin, G., Wang, S., Dai, N., Li, Y., Liu, J., Rehtanz, C., ... & Zhou, Y. (2024). A Reduced-Order Impedance Model and Analytical Loop-Correction Stabilization Method for Electric Vehicle DC Charging Station. *IEEE Transactions on Power Delivery*, 39(4), 2194-2206.

Mateen, S., Amir, M., Haque, A., & Bakhsh, F. I. (2023). Ultra-fast charging of electric vehicles: A review of power electronics converter, grid stability and optimal battery consideration in multi-energy systems. *Sustainable Energy, Grids and Networks*, 35, 101112.

Mishra, D., Singh, B., & Panigrahi, B. K. (2022). Sigma-modified power control and parametric adaptation in a grid-integrated PV for EV charging architecture. *IEEE Transactions on Energy Conversion*, 37(3), 1965-1976.

Mohammed, A. M., Alalwan, S. N. H., Taşcıkaraoğlu, A., & Catalão, J. P. (2022). Sliding mode-based control of an electric vehicle fast charging station in a DC microgrid. *Sustainable Energy, Grids and Networks*, 32, 100820.

Narthana, S., & Gnanavadivel, J. (2024). Power quality analysis of interleaved cuk configuration-based interval type-2 fuzzy logic controller for battery charging in electric vehicles. *Arabian Journal for Science and Engineering*, 49(5), 6259-6273.

Safiullah, S., Rahman, A., & Lone, S. A. (2021). State-observer based IDD controller for concurrent frequency-voltage control of a hybrid power system with electric vehicle uncertainties. *International*

Transactions on Electrical Energy Systems, 31(11), e13083.

Sepehrzad, R., Khodadadi, A., Adinehpour, S., & Karimi, M. (2024). A multi-agent deep reinforcement learning paradigm to improve the robustness and resilience of grid connected electric vehicle charging stations against the destructive effects of cyber-attacks. *Energy*, 307, 132669.

Shi, K., Tang, C., Long, H., Lv, X., Wang, Z., & Li, X. (2021). Power fluctuation suppression method for EV dynamic wireless charging system based on integrated magnetic coupler. *IEEE Transactions on Power Electronics*, 37(1), 1118-1131.

Shi, K., Tang, C., Wang, Z., Li, X., Zhou, Y., & Fei, Y. (2022). A magnetic integrated method suppressing power fluctuation for EV dynamic wireless charging system. *IEEE Transactions on Power Electronics*, 37(6), 7493-7503.

Singh, A. R., Vishnuram, P., Alagarsamy, S., Bajaj, M., Blazek, V., Damaj, I., ... & Othman, K. M. (2024). Electric vehicle charging technologies, infrastructure expansion, grid integration strategies, and their role in promoting sustainable e-mobility. *Alexandria Engineering Journal*, 105, 300-330.

Suresh, P., Kalirajan, K. K., Soundarapandian, K. A., & Nadar, E. R. S. (2024). Performance evaluation of improved Y source power factor correction converter with enhanced power quality in EV rapid charger application. *Electrical Engineering*, 106(4), 4787-4805.

Tirunagari, S., Gu, M., & Meegahapola, L. (2022). Reaping the benefits of smart electric vehicle charging and vehicle-to-grid technologies: Regulatory, policy and technical aspects. *IEEE Access*, 10, 114657-114672.

Wang, L., Qin, Z., Slangen, T., Bauer, P., & Van Wijk, T. (2021). Grid impact of electric vehicle fast charging stations: Trends, standards, issues and mitigation measures-an overview. *IEEE Open Journal of Power Electronics*, 2, 56-74.

Yang, R. H., Jin, J. X., Chen, X. Y., Zhang, T. L., Jiang, S., Zhang, M. S., & Xing, Y. Q. (2022). A battery-energy-storage-based DC dynamic voltage restorer for DC renewable power protection. *IEEE Transactions on Sustainable Energy*, 13(3), 1707-1721.

Zand, M., Alizadeh, M., Nasab, M. A., Nasab, M. A., & Padmanaban, S. (2024). Electric vehicle charger energy management by considering several sources and equalizing battery charging. *Renewable Energy Focus*, 50, 100592.